Renewable Energy 140 (2019) 943–956

Contents lists available at ScienceDirect

Renewable Energy

journal homepage: www.elsevier.com/locate/renene

A hybrid strategy combining minimized leading-edge electric-heating and superhydro-/ice-phobic surface coating for wind turbine icing mitigation

Linyue Gao, Yang Liu, Liqun Ma, Hui Hu*

Department of Aerospace Engineering, Iowa State University, Ames, IA, 50011-2271, United States

ARTICLE INFO

Article history:
Received 12 July 2018
Received in revised form
2 January 2019
Accepted 24 March 2019
Available online 27 March 2019

Keywords:
Wind turbine icing phenomena
Wind turbine anti-/de-icing
Electric heating
Superhydrophobic surface
Icing wind tunnel testing

ABSTRACT

A hybrid anti-icing strategy that combines minimized electro-heating at the blade leading edge and a superhydro-/ice-phobic coating to cover the blade surface was explored for wind turbine icing mitigation. The experimental study was conducted in an Icing Research Tunnel available at Iowa State University (ISU-IRT) with a turbine blade model with DU91-W2-250 airfoil in the model cross-section exposed under different icing conditions. While a superhydro-/ice-phobic surface coating was used to cover the entire blade surface, a strip of electric heating film was used to wrap around the leading edge of the blade model. By using the superhydro-/ice-phobic coating to cover the entire blade surface, the hybrid strategy with the electric heating element covering only 5%–10% of the blade front surface would be able to keep the entire blade surface ice free under both rime and glaze icing conditions. In comparison to the conventional strategy to brutally heating the entire hydrophilic blade surface to keep the blade ice free, the hybrid strategy was found to be able to achieve the same anti-/de-icing performance with substantially less power consumption (i.e., up to ~90% saving in the required power consumption), making it a very promising strategy for wind turbine icing mitigation.

1. Introduction

Wind energy is the most promising clean and renewable energy that can be used to generate electricity [1]. According to a report published by British Petroleum Global, wind power generation reaches 960 TWh with an increment of 15.6% in 2016, providing approximately 4% of the total electricity generation in the world [2]. In Demark, wind turbines deliver 44% of the total electricity consumption of the country in 2017. With the surge of wind energy installations, cold climate areas become more and more attractive to wind farm developers due to the abundant wind resources and relatively low population densities in the areas. As described in the report of Lehtomaki [3], Global wind power generation in cold climates is approximately 127 GW by the end of 2015, with a promising forecasted annual growth of 12 GW from 2016 to 2020. 72%, 94% and 19% of the wind turbines have the opportunity to encounter various icing events in climate regions of North America, Europe, and Asia, respectively [3]. Wind turbine icing has been found to pose tremendous threats to the integrity and safe operation of the wind turbines. Accumulated ice on wind turbine blades can significantly alter the geometric shapes and increase the surface roughness, resulting in dramatic aerodynamic performance degradations of the turbine blades, and accounting for up to 30% of the annual energy production (AEP) [4–6]. The uneven distributions of ice accreted over the turbine blade surfaces in both spanwise and chordwise directions would add additional loadings or vibrations to the turbine rotors, which can greatly threaten the health of wind turbine components and shorten the operation lifetime of the wind turbines [7,8]. The secondary effects, including the increased noise and the sudden shedding/fall of large ice chucks [9,10], could seriously affect human life and property security in the neighboring area. Therefore, it is highly desirable and urgently needed to develop effective solutions for wind turbine icing mitigation.

While a number of anti-/de-icing systems have been used for wind turbine icing mitigation [11–15], almost all the current anti-/de-icing strategies were originally developed for aircraft anti-/de-icing applications. The anti-/de-icing methods can usually be divided into two categories: i.e., passive methods and active

* Corresponding author.
E-mail address: huhui@iastate.edu (H. Hu).

https://doi.org/10.1016/j.renene.2019.03.112
0960-1481/

methods. The passive methods, including ice-phobic/hydrophobic coatings [10,16–26], black paintings [16], and operation stops, are usually used for anti-icing purposes to prevent or delay ice formation over wind turbine surfaces. The active methods usually require external energy input for anti-/de-icing operation, which include surface heating methods (e.g., hot air injection, resistive heating, microwave heating [27], and plasma heating [28,29]), mechanical actuation methods (e.g., inflated rubber boots [16,30,31]), chemical spray methods (e.g., spraying low-freezing-point anti-icing liquids), and active pitch control methods [32,33].

Among various active anti-/de-icing methods, surface heating methods are considered to be the most efficient approaches to prevent ice formation/accretion over the turbine blade surface. Hot air injection and electric heating are the two most-commonly-used surface heating methods for wind turbine icing mitigation [3,12]. Hot air injection systems, first commercialized by ENERCON in 2011 [34], use hot airflow circulating inside the hollow turbine blades for icing mitigation. However, due to the low thermal conductivity of the composite materials used to make wind turbine blades, hot air injection systems were found to lead to a great deal of energy loss during the anti-/de-icing operation. In comparison to the hot air injection methods, resistive electric heating methods (i.e., electric heating over outer surfaces of turbine blades) are found to have a comparatively low energy consumption and high flexibility in installation for both existing and newly-developed wind turbines [3,12]. However, as the dimension of the turbine blades increases, the required energy consumption by using the electric heating methods would increase dramatically. In order to ensure most of the electricity generated by wind turbines can be integrated into the power grid, instead of being consumed locally to brutally heat the blade surfaces for anti-/de-icing operation, it is highly desirable to develop novel and effective anti-/de-icing strategies with minimized power consumption for the anti-/de-icing operation.

Due to the low installation cost and almost zero energy consumption, passive anti-icing approach with hydro-/ice-phobic surface coatings attract more and more attention recently as a viable strategy for wind turbine icing mitigation. Inspired by the outstanding self-cleaning capability of lotus leaf and duck feather, extensive studies have been conducted in recent years to develop coatings to make ***S**uper-**h**ydrophobic **S**urfaces* (**SHS**) [10,19–23,35], on which water droplets bead up with a very large contact angle (i.e., >150°) and drip off rapidly when the surface is slightly inclined. One attractive application of SHS, in addition to the extraordinary water-repellency, is their potentials to reduce snow/ice accumulation on solid surfaces. Under a frost-free environment (i.e., low humidity conditions), SHS was found to show promising behaviors in delaying ice formation [36,37] even at temperatures as low as −25 to −30 °C [35,38–47]. Gao et al. [48] studied the anti-icing properties of SHS coatings over an aluminum plate under both laboratorial and natural icing conditions, and confirmed that SHS could alleviate ice formation/accretion to some extent. Mangini et al. [49] investigated the mechanism of runback ice formation on a superhydrophobic surface, and found that surface wetting property could dramatically change the ice formation process. More recently, Khedir et al. [40] conducted a comprehensive review to summarize the recent research progress on the development of various superhydrophobic surfaces and their applications for icing mitigation. Other passive anti-icing approaches, such as using slippery liquid-infused porous surfaces (SLIPS) [43,50,51] and soft PDMS materials [52], have also been explored under various icing conditions in recent years. As demonstrated by Liu et al. [52] and Waldman et al. [53], for airfoil/wing models coated with hydro-/ice-phobic coatings, ice formation/accretion would be mitigated greatly since the aerodynamic forces exerted from the boundary layer airflows would sweep away the water/ice away from most of the SHS coated airfoil/wing surfaces. However, ice was still found to form in the vicinity of the stagnation line near the airfoil/wing leading edge. The findings indicate that no passive anti-icing approaches with hydro-/ice-phobic surface coatings would be able to prevent ice formation/accretion over the airfoil surface completely [52]. This highlights one of the major challenges facing hydro-/ice-phobic coating strategies. The hydro-/ice-phobic coatings could produce low adhesion forces between the surface and water/ice and rely on aerodynamic shear forces acting tangentially to the surface to remove the water/ice accretion. Such passive approaches would break down near the stagnation line because the required shear forces near the stagnation line are very small or completely vanishes. Further exacerbating the problem is that the water collection efficiency is a maximum at the airfoil stagnation line.

Advancing the technology for safe and efficient operation of wind turbines under atmospheric icing conditions requires the development of novel, effective and low-power anti-/de-icing strategies for wind turbine icing mitigation and protection. In the present study, we report the research progress made in our recent efforts to explore a novel hybrid anti-/de-icing strategy by combining the passive anti-icing method with water/ice repellent superhydrophobic surface (SHS) and minimized surface heating near blade leading edge for wind turbine icing mitigation. The hybrid anti-/de-icing strategy was experimentally evaluated and compared quantitatively with other conventional passive and active anti-/de-icing strategies in terms of effectiveness and required power consumption for the anti-/de-icing operation. The explorative study was conducted by using a unique Icing Research Tunnel available at Iowa State University (ISU-IRT) to generate both wet glaze and dry rime icing conditions to be representative of the typical icing conditions experienced by wind turbines when operating in cold climates. A composited-based turbine blade model with DU91-W2-250 airfoil shape in the model cross-section was manufactured and mounted in the test section of ISU-IRT to evaluate the effectiveness of hybrid anti-/de-icing strategy for wind turbine icing mitigation. During the experiments, while a high-speed imaging system was used to record the dynamic ice accretion processes on the turbine blade model, an infrared (IR) thermal imaging system was utilized to map the surface temperature distributions during the dynamic anti-/de-icing operation. A parametric study was also performed in order to explore/optimize the design paradigms of the hybrid anti-/de-icing strategy in order to minimize the power consumption needed for the anti-/de-icing operation.

2. A brief description of the hybrid anti-/de-icing strategy

Wind turbine anti-/de-icing operation refers to prevent ice formation/accretion over the surfaces of turbine blades. As described above, it can be effectively achieved by using active approaches to electrically heat the blade surfaces either in an evaporative regime in which the blade surface is heated up to over 100 °C to evaporate all the impinged super-cooled water droplets [54] or a wet water runback regime in which the impinged super-cooled water droplets are heated up to a “warmed” state (i.e., at the temperature greater tha n the water frozen temperature) in order to remain in liquid phase [12]. The evaporative regime requires an extremely high-power input to the electric heating element in order to maintain the heated blade surface at a high temperature over 100 °C under atmospheric icing conditions, which might also cause unexpected over-heating issues to the composite-based turbine blade epoxy. In comparison to the evaporative regime, the wet water runback regime is much safer and energy-saving, thus, is preferred and selected in the present study.

When operating in the wet water runback regime, the impacted

water mass would accumulate over the blade surface and run back over the blade surface as driven by the boundary layer airflow. Since the "warmed" surface water would be cooled down rapidly as running back over the frozen-cold blade surface and may be refrozen in ice over the blade surface, it usually requires the entire blade surface to be heated in order to avoid the refreezing of the runback water in the downstream region beyond the area protected by the electric heating element. As described in the recent study Gao et al. [55], due to the much stronger convective heat transfer near the airfoil leading-edge (LE), it would require a much greater power input to prevent ice formation/accretion in the region near the blade leading edge, in comparison to those over the downstream regions, for the anti-/de-icing operation. Since the super-cooled water droplets would be impacting onto the blade surface mainly in the region near the blade leading edge, i.e., within the droplet impinging limit near the airfoil leading edge as described in Papadakis et al. [56], LE heating is essential to prevent ice formation/accretion upon the impacting of the supercooled water droplets onto the turbine blades. The main challenge for the LE heating-based strategy is how to prevent refreezing of the runback surface water at the downstream region of the turbine blade surface. Since the composite-based turbine blade surfaces are typically hydrophilic, the moving speed of the runback surface water is usually relatively slow with a bigger wetted area over the hydrophilic blade surface. One commonly used method to prevent refreezing of the runback surface water over the hydrophilic blade surface is to extend the size of the area protected by the electric heating element, i.e., brutally heating a much greater area over the blade surface to enable the runback surface water to stay in liquid phase until shedding off for the blade trailing edge (TE). Such a solution could lead to a massive heated area over the turbine blade, i.e., up to 100% of the hydrophilic blade surface, in order to keep the entire blade surface free of ice, thereby, resulting in a very high power consumption for the anti-/de-icing operation.

As reported in the recent studies of Waldman et al. [53] and Liu et al. [57], in comparison to those over hydrophilic surfaces, the capillary forces and/or ice adhesion strength over superhydrophobic-/ice-phobic surfaces would become much smaller. As driven by the same magnitude of the aerodynamic force tangential to the surfaces, the surface water or ice/water mixture would runback much faster over superhydrophobic-/ice-phobic surfaces than that over hydrophilic surfaces. Therefore, another more promising solution to prevent the formation of runback ice over the turbine blade surface is to coat the entire turbine blade surface with a superhydrophobic-/ice-phobic coating, which could make the surface water move much faster over the blade surface and roll off swiftly from the turbine blade before being refrozen into ice.

With this in mind, we conducted the present study to explore/evaluate a hybrid anti-/de-icing strategy that combines an active LE heating method and a passive SHS coating method for wind turbine mitigation. Fig. 1 shows the configuration of the hybrid anti-/de-icing strategy. In the present study, while the turbine blade model without any surface treatments was used as the comparison baseline (i.e., the 1st layer in Fig. 1), an electric heating film was used to wrap around the leading edge of the blade model in order to heat up the impacted super-cooled water droplets to effectively avoid ice formation/accretion within the impacting region near the blade leading edge (i.e., 2nd layer in Fig. 1). A spray-on SHS coating was then applied onto the outmost layer of the turbine blade model (i.e., 3rd layer in Fig. 1) to bounce off the impinging water droplets near the blade leading edge and to reduce the capillary force/ice adhesion strength of the runback water/ice mixtures over the blade surface in order to prevent refreezing of the runback surface water with a much smaller power consumption for wind turbine icing mitigation.

3. Experimental setup and test model

3.1. ISU-IRT used in the present study

The experimental study was performed in the unique Icing Research Tunnel available at Iowa State University (i.e., *ISU-IRT*), which is a newly-refurbished, multifunctional icing research tunnel. As shown schematically in Fig. 2, ISU-IRT has a test section with four optically transparent side walls and its dimension of 2.0 m in length × 0.4 m in width × 0.4 m in height. It has a capacity of generating a maximum wind speed of 100 m/s and airflow temperature down to $-25°C$. An array of pneumatic atomizers/spray nozzles (Spraying Systems Co., 1/8NPT-SU11) were installed at the entrance of the contraction section of ISU-IRT to generate micro-

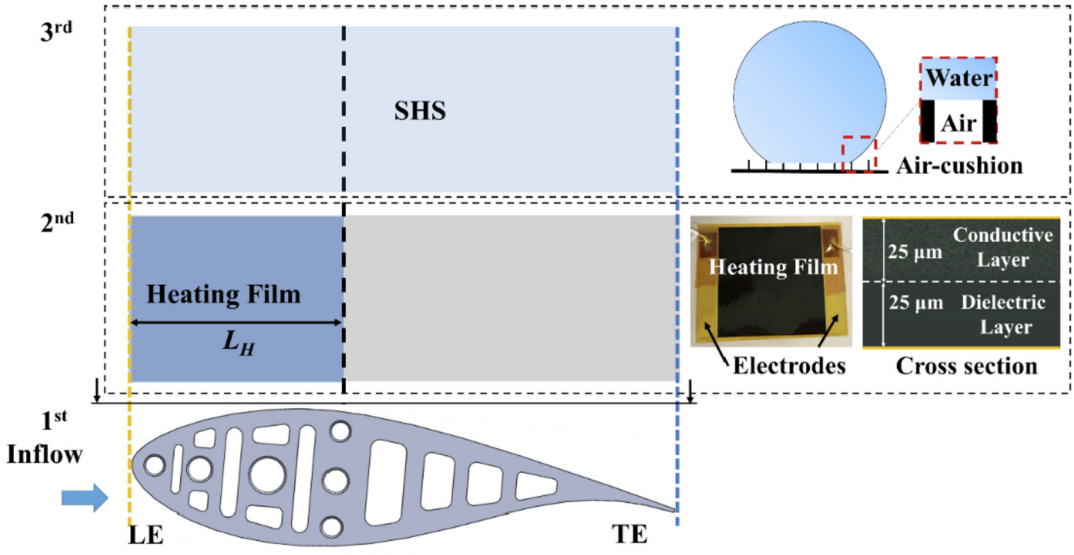

Fig. 1. Schematic of the hybrid anti-/de-icing strategy to be explored in the present study.

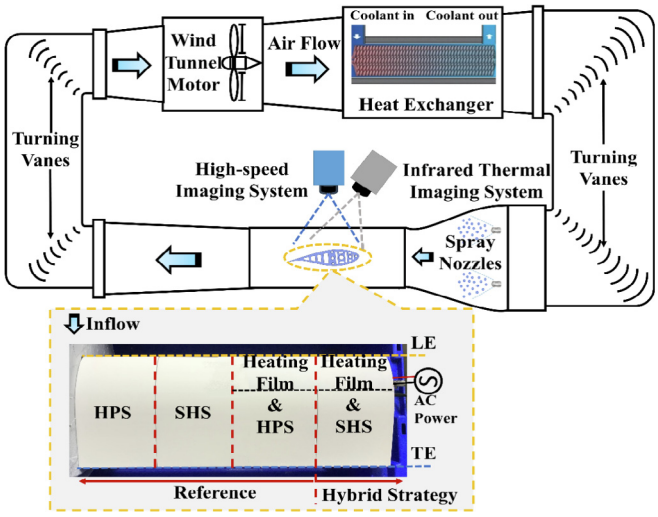

Fig. 2. Schematic of ISU-IRT and experimental setup to evaluate the effectiveness of various anti-/de-icing strategies.

sized water droplets with a medium volumetric diameter (MVD) ranging from 10 μm to 100 μm. The desired MVD and liquid water content (LWC) in ISU-IRT can be achieved by adjusting the air/water pressure and the flowrate supplied to the atomizers/spray nozzles. In summary, ISU-IRT is capable to duplicate a wide range of atmospheric icing conditions, i.e., from dry rime to very wet glaze icing conditions representative of typical wind turbine icing envelope [32,58–60]. Further technical details about ISU-IRT can be found in the published literature of Gao et al. [33] and Liu et al. [61].

3.2. The turbine blade model used in the present study

A wind turbine blade section model with DU91-W2-250 airfoil profile in the cross section was manufactured for the present study. DU91-W2-250 airfoil profile was widely used for wind turbine blade design due to its favorable aerodynamic performance and structural properties [62,63]. The turbine blade model is 0.15 m in airfoil chord length (i.e., $C = 0.15$ m) and 0.40 m in spanwise length, which fits nicely into the test section of ISU-IRT. The turbine blade model was 3D-printed with a hard plastic material (i.e., VeroWhitePlus), which represents well to the composite-based materials used to make wind turbine blades. The 3D-printed blade model was coated with several layers of spray-on primer, and then sanded with up to 2000 grid fine sandpapers to achieve a very smooth finish. An all-weather protective spray-on enamel coating (Rustoleum™, Flat Protective Enamel, white in color) was coated onto the sanded model surface to achieve the commonly-used surface for wind turbines, i.e., hydrophilic surface (HPS).

As shown schematically in Fig. 2, the turbine blade model was divided into four distinct sections along the spanwise direction in order to provide a side-by-side comparison of different anti-/de-icing strategies, including 1) the turbine blade model with hydrophilic surface (i.e., HPS case), 2) the turbine blade model with coated with a SHS coating (i.e., SHS case); 3) the turbine blade model wrapped with an electric heating film at the blade leading edge but coated with a hydrophilic surface coating over the blade surface (i.e., LE heating only case); and 4) the hybrid strategy that combines the LE heating and a SHS coating to cover the entire blade surface (i.e., hybrid case). In the present study, the HPS case is representative of conventional wind turbine blade surfaces, which is the baseline for the comparative study. The SHS case was produced by spraying a commercially-available superhydrophobic coating (i.e., with Hydrobead™ Standard with Hydrobead ™ Enhancer) to cover the entire blade surface. In the present study, the LE heating was achieved by using a thin electric heating film (i.e., DuPont™ Kapton® RS with a film thickness of 50 μm) to cover the leading edge of the turbine blade model. The thin heating film has a good heat uniformity and design flexibility, which can easily wrap around the leading edge of the blade model for anti-/de-icing purpose. The hybrid strategy case was achieved by combining the LE heating along with SHS coating at the outmost layer of the blade model surface, as shown schematically in Fig. 1.

In the present study, the electric heating element was powered by an alternative current (AC) power supply. The output voltage and electric current supplied to the electric heating element were measured with a multi-meter, and the measured values were used to determine the required power consumption for the anti-/de-icing operation. In order to determine the minimum value of the required power input for successful anti-/de-icing operation (i.e., to prevention ice formation/accretion over the entire surface of the turbine blade model), a series of experiments were conducted by carefully adjusting the power input supplied to the electric heating element. The power input was first set to a comparatively high value (e.g., 5 kW/m^2 for glaze, while 10 kW/m^2 for rime) to keep the entire surface of the blade model completely ice free. Then, the power input supplied to the electric heating element was slightly decreased by an interval of 0.3 kW/m^2 until observable ice structure was found to accrete over the surface of the blade model. The smallest value of the power input required for successful anti-/de-icing operation (i.e., keep the entire surface of the turbine blade model ice-free) was recorded as the required minimum power consumption for the test case.

3.3. Experimental parameters used in the present study

It is well known that, the ice accretion process over the surface of wind turbine blades can be either glaze icing (i.e., only a portion of the super-cooled water droplets freeze into ice upon impacting onto the blade surface) and rime icing process (i.e., all the impacted super-cooled water droplets freeze into ice immediately upon impacting onto the blade surface) depending on the combined effects of ambient temperature, wind speed, size of the supercooled water droplets, and Liquid Water Content (LWC) level in the airflow [15,61,64]. In order to evaluate the effectiveness of various anti-/de-icing strategies under typical atmospheric icing conditions experienced by wind turbines, both a typical glaze icing condition (i.e., $V_\infty = 40$ m/s, $T_\infty = -5$ °C, and LWC = 2.0 g/m^3) and a typical rime icing condition (i.e., $V_\infty = 40$ m/s, $T_\infty = -10$ °C, and LWC = 0.4 g/m^3) were generated in ISU-IRT for the present study. For each test cases, ISU-IRT was operated at a pre-scribed frozen cold temperature level (e.g., $T_\infty = -5$ °C for glaze icing and $T_\infty = -10$ °C for rime icing) for at least 20 min under a dry airflow condition (i.e., without turning on the water spray system of ISU-IRT) to ensure that ISU-IRT reached a thermal steady state. After the electric heating element was switched on for approximately 150 s to reach a relatively stable working condition, the water spray system of ISU-IRT was then turned on to start a 600-s icing experiment in order to evaluate the effectiveness of various anti-/de-icing strategies for wind turbine icing mitigation.

In the present study, the turbine blade model was mounted in the middle of the test section of ISU-IRT via a stainless-steel rode at its ¼ chord, i.e., at the aerodynamic center of the blade model. The turbine blade model can be adjusted to the desired angle of attack (AoA) by pivoting the airfoil model about the supporting stainless-steel rod as measured with a digital angle gauge. For the present study, the turbine blade model was set to be at the angle of attack (AOA) of 5° (i.e., AOA = 5°, at the angle with the maximum lift-to-drag ratio for the DU91-W2-250 airfoil), which would be

representative of the wind turbine blade operating under the most efficient operation condition.

It should be noted that, the effects of the gravity of the impinging super-cooled water droplets on the dynamic ice accreting process over the turbine blade model were carefully assessed in the present study by using a nondimensional Froude number (i.e., $Fr = V_\infty / \sqrt{gC}$, where V_∞ is the incoming airflow velocity, g is the constant of the gravitational field, and C is the chord length of the turbine blade model). It was found that the influence of the gravity of the impinging water droplets on the dynamic icing process is negligible (i.e., <1.0%) for the test cases of the present study.

3.4. High-Speed imaging system and Infrared (IR) thermal imaging systems used in the present study

During the experiments, a high-speed video imaging system (PCO Tech, Dimax™ with acquisition rate up to 25,000 frames per second at the spatial resolution of 1008 pixels by 1008 pixels) was installed right above the turbine blade model to provide a top view visualization of the anti-/de-icing processes. The spatial resolution of the recorded high-speed images is 11.3 pix/mm. A high-speed infrared (IR) thermal imaging system (FLIR, A615) was also utilized to quantitatively measure the surface temperature distribution over the surface of the turbine blade model during the anti-/de-icing operation. For the IR thermal imaging, an infrared window (FLIR, IR Window-IRW-4C) was embedded into the top panel of the ISU-IRT test section. The spatial resolution of the acquire IR thermal images is 4.0 pix/mm. It should be noted that, the IR emissivity of water, ice and enamel covered the turbine blade model surface are 0.95, 0.98 and 0.96, respectively [65], which were used to correct the IR thermal imaging results. In the present study, two miniaturized K-typed thermocouples were also slush mounted on the upper surface of the turbine blade model in order to validate the IR thermal imaging results. The measurement data acquired from the thermocouples and the IR thermal imaging system were compared quantitatively, showing in a good agreement with an uncertainty less than ±0.5 °C.

4. Measurement results and discussions

4.1. Effects of the surface properties of the turbine blade model

It is well known that, during a wind turbine icing event, the aerodynamic shear force acting on an ice structure accreted over the surface of a wind turbine blade would be resisted by the ice adhesion strength between accreted ice structures and the blade surfaces. A small ice adhesion strength over the blade surface is highly desired for anti-/de-icing purpose. In the present study, by using a measurement technique similar to the one described in Meuler et al. [66], the ice adhesion strengths over the hydrophilic surface of the turbine blade model and the SHS coated blade surface were measured, and the measurement results were given in Table 1. The mean and standard deviation values given in the table were calculated based on 10 trials of the measurements. As shown clearly in Table 1, the ice adhesion strength on the original hydrophilic blade surface and the SHS-coated blade surface are found to be 1.40 MPa and 0.37 MPa, respectively, which are within the range of the ice adhesion strength values reported in the article of Kreder et al. [50] and Edalatpour et al. [67]. It should be noted that, the ice adhesion strength on the SHS coated blade surface was found to be only ~25% of that over the original hydrophilic surface of the turbine blade model.

Surface wettability, which is characterized by the contact angles of a water droplet on a solid surface, is used to describe the ability of a water droplet to maintain contact with the solid surface. It is usually also used to indicate the water repellency of the surface. In the present study, the contact angles of sessile water droplets over the original hydrophilic blade surface (i.e., HPS case) and the SHS coated blade surface (i.e., SHS case) were measured using a similar procedure as described in Waldman et al. [53]. As shown clearly in Fig. 3, the contact angle of the water droplet sitting on the original hydrophilic blade surface is obviously smaller than 90° (i.e., $\theta \approx 65°$ for the hydrophilic surface of the present study). The measured contact angle of the water droplet on the SHS coated blade surface was found to be about 157° (i.e., $\theta \approx 157°$). By using a similar needle-in-the-sessile-drop-method as that described in Korhonen et al. [68], the receding and advancing angles of water droplets (i.e., θ_{adv} and θ_{rec}) over the two compared surfaces were also measured, and the measurement results were summarized in Table 1.

To have a more quantitative comparison about the effects of the surface wettability on icing process, especially for glaze icing process, the capillary forces that resist the water droplets sliding/rolling on the two compared surfaces were also calculated based on as a theoretical model derived in Waldman et al. [59], which is expressed in Eq. (1).

$$F_{capillary} \approx \pi R \gamma_{LG} \left[\sin\left(\frac{\theta_{adv} - \theta_{rec}}{2}\right) \sin\left(\frac{\theta_{adv} + \theta_{rec}}{2}\right) \right] \quad (1)$$

where R is the spherical cap radius of the water droplet, and γ_{LG} is the liquid-gas surface tension at the contact line. θ_{adv} and θ_{rec} represent the advancing and receding contact angles, respectively.

By putting the measured advancing and receding contact angles listed in Table 1 into Eqn. (1), the ratio of the capillary forces over the two compared surfaces can be estimated, as shown in Eq. (2). It can be seen clearly that, the capillary force acting a water droplet on the SHS coated blade surface is much smaller, i.e., only about 4.0% of that on the original hydrophilic surface of the turbine blade model,

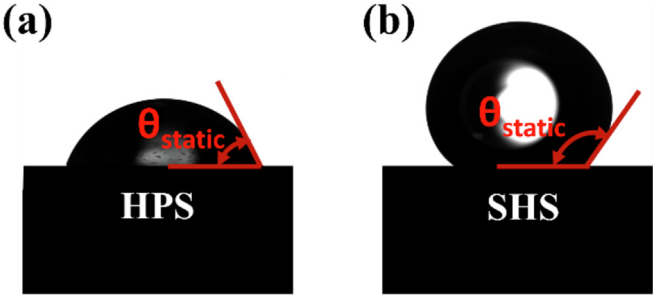

Fig. 3. Acquired images of the water droplets sitting on (a). original hydrophilic blade surface, and (b). SHS coated blade surface.

Table 1
Surface properties of various surfaces.

Surface	Ice Adhesion Strength [MPa]	Static contact angle θ_{static} [°]	Advancing contact angle θ_{adv} [°]	Receding contact angle θ_{rec} [°]	Hysteresis $\Delta\theta$ [°]
HPS	1.40 ± 0.13	65 ± 2	105 ± 2	50 ± 2	>50
SHS	0.37 ± 0.09	157 ± 2	159 ± 2	154 ± 2	<5

$$\frac{F_{cap,SHS}}{F_{cap,HPS}} \approx \frac{\left[\sin\left(\frac{\theta_{adv}-\theta_{rec}}{2}\right)\sin\left(\frac{\theta_{adv}+\theta_{rec}}{2}\right)\right]_{SHS}}{\left[\sin\left(\frac{\theta_{adv}-\theta_{rec}}{2}\right)\sin\left(\frac{\theta_{adv}+\theta_{rec}}{2}\right)\right]_{HPS}} \approx 0.04 \quad (2)$$

It is well known that the dynamics of the droplet impinging process can also affect the ice accretion process over the turbine blade surface significantly. Similar as that described in Liu et al. [52], a vertical wind tunnel was used to in the present study accelerate water droplets of ~3.0 mmm in size to a comparatively high impacting speed (i.e., to reach a high impacting Weber number of $We \approx 3000$) in order to simulate the dynamic impinging process of supercooled water droplets pertinent to wind turbine icing phenomena. Further information about the vertical wind tunnel and experimental setup for the water droplet impingement experimental is available in Liu et al. [52].

Fig. 4 shows the time sequences of the acquired snapshot images to reveal the dynamic impinging processes of water droplets onto the hydrophilic blade surface and SHS-coated blade surface (i.e., HPS case vs. SHS case) at a comparatively high Weber number of ~3100. It can be seen clearly that, when a water droplet impacted onto the hydrophilic blade surface, it would spread out in all directions to form "pancake-like" structure over the hydrophilic surface with the certain splashing of tiny water droplets at the boundary rim. As times goes by, the "pancake-like" structure would continue to spread out until reaching its maximum diameter, as shown in Fig. 4(a). After that, the "pancake-like" structure would start to go through a receding process with the impacted water mass flowing from the spreading boundary back to the impinging center. In summary, upon impacting of the water droplet onto the hydrophilic surface, the impacted water would spread out rapidly to form "pancake-like" structure (i.e., a thin water film with a much larger contact area in comparison to the diameter of the water droplet) over the hydrophilic surface with most of the impacted water mass still remaining on the hydrophilic surface after the impinging process.

In comparison to the spreading-receding process of the water droplet onto the hydrophilic surface, the dynamics of the droplet impinging process onto the SHS-coated blade surface was found to become much more involved, as shown clearly in Fig. 4(b). After the water droplet impinged onto the SHS-coated blade surface, it would spread out rapidly to form a thin water film over the impacted surface. However, instead of forming "pancake-like" thin water film over the impacted surface, the out-spreading water film was found to break into many tiny droplets, and bouncing off from the impacted surface immediately and splashing into the ambient air over the impacted surface, due to the existence of the nano-/micro-scale roughness/textures on the SHS-coated surface. As a result, upon dynamic impacting of the water droplet, most of the impacted water mass would be rebounding off from the surface, and only a small portion of the impacted water mass was found to remain on the impacted surface at the end of the impinging process. As shown clearly in Fig. 4(b), even the remaining water mass would bead up over the SHS-coated surface with a much larger contact angle (i.e., $\theta > 150^{\circ}$) and a considerably small contact area.

4.2. Comparison of the anti-/de-icing performance of various strategies

In the present study, a successful anti-/de-icing operation is defined as no ice structures would be able to accrete over the turbine blade surface during the anti-/de-icing process. The entire surface of the turbine blade model covered with an electric heating film element (i.e., 100% surface heating) is selected as the reference for a further comparison of the power consumptions needed for the compared anti-/de-icing strategies. Fig. 5 shows the examples of the successful anti-/de-icing operation by using 100% surface heating under both the wet glaze icing condition (i.e., $V_{\infty} = 40$ m/s; $T_{\infty} = -5\,^{\circ}$C; $LWC = 2.0$ g/m^3) and dry rime icing condition (i.e., $V_{\infty} = 40$ m/s; $T_{\infty} = -10\,^{\circ}$C; $LWC = 0.4$ g/m^3). The minimum required power consumption for preventing glaze and rime ice formation over the blade model were found to 3.20 kW/m^2 and 6.80 kW/m^2, respectively, for the strategy to heat entire blade surface (i.e., 100% surface heating). Under the wet glaze icing condition, the impacted supercooled water droplets were found to be heated up to stay in liquid phase, forming a thin water film over the surface of the

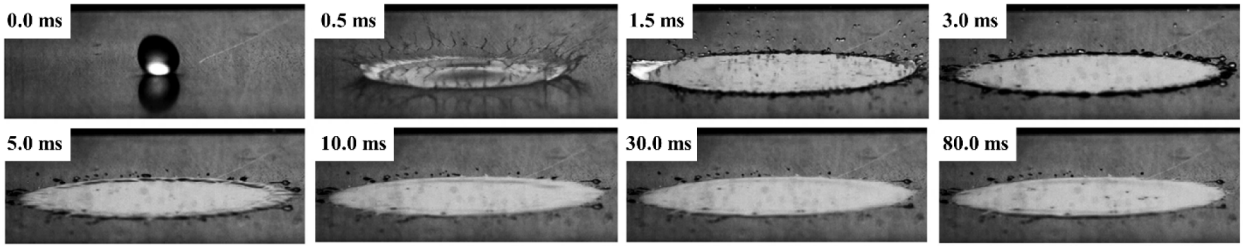

(a) Dynamic impingement of a water droplet onto hydrophilic blade surface (i.e., HPS case).

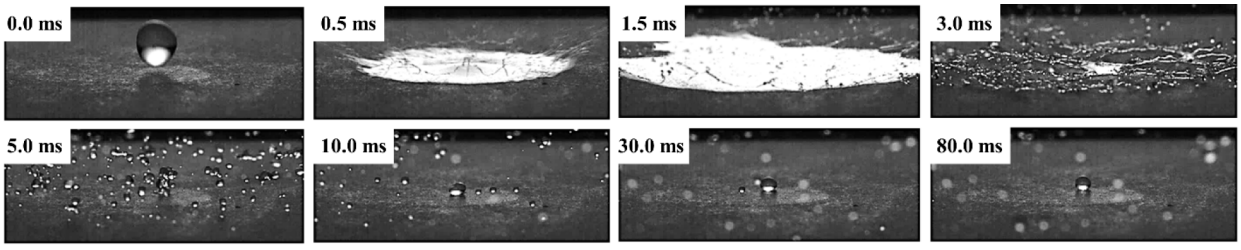

(b) Dynamic impingement of a water droplet onto the SHS -coated blade surface (i.e., SHS case).

Fig. 4. Time-evolutions of the dynamic impinging process of water droplets onto the blade surface for the HPS cases and SHS case at a relatively high Weber number of $We \approx 3100$.

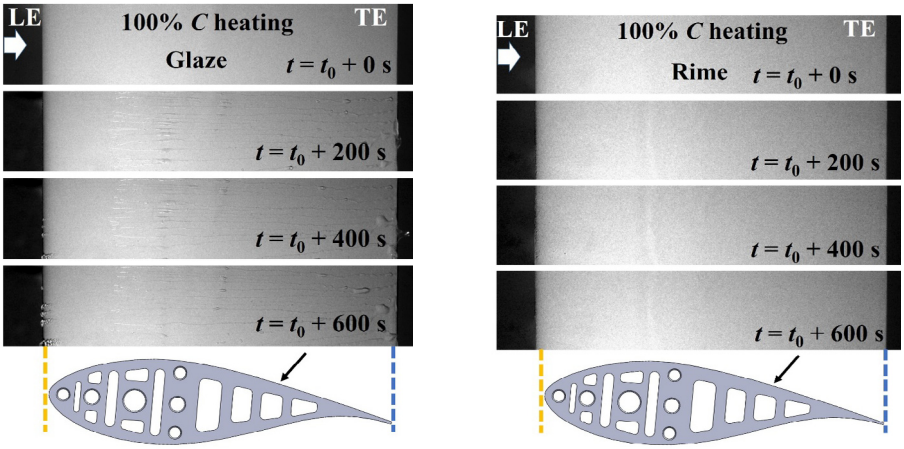

(a) (a). Glaze icing condition ($P.D._H$ = 3.20 kW/m^2) (b). Rime icing condition ($P.D._H$ = 6.80 kW/m^2)

Fig. 5. Snapshot images of the successful anti-icing operation with the entire blade surface heating strategy under the typical glaze and rime icing conditions.

turbine blade model near the blade leading edge. The impacted water mass over the blade surface was found to run back rapidly as driven by the boundary layer airflow. The runback water film was found to split into multiple water rivulets at downstream location, and finally shed off from the trailing edge of the turbine blade model, as shown clearly in Fig. 5(a). A similar process is also expected under the rime icing condition. It should be noted that, in comparison to the case under the glaze icing condition, the impingement of the super-cooled water droplets within a certain time would be much less for the rime icing case due to the much low *LWC* level. As shown in Fig. 5(b), most of the impinged water droplets were found to be evaporated upon impacting onto the heated blade surface near the leading edge, therefore, no obvious surface water runback was observed for the rime icing case. It should be noted that, the surface temperature of the unloaded turbine blade model (i.e., for the test case with $V_\infty = 0$ m/s) was found to be quite uniform due to the high thermal uniformity of the electric heating film used in the present study. During the anti-/de-icing experiment, the surface temperature near the blade leading edge was found to be relatively lower in comparison with downstream regions, due to the stronger convective heat transfer near the airfoil leading edge. As described in Gao et al. [55], the required power consumption for the entire blade surface heating strategy (i.e., 100% surface heating) would be mainly determined by the anti-/de-icing process around the leading edge of the turbine blade model.

Fig. 6 and Fig. 7 show the acquired snapshot images to reveal the anti-/de-icing effectiveness of the hybrid strategy in comparison with other conventional anti-/de-icing strategies under the same glaze and rime icing conditions. The dynamic ice accretion process over the surface the turbine blade model without using any anti-/de-icing methods (i.e., the HPS case as the for the comparison baseline) under the same glaze and rime icing conditions are also shown in the figures to reveal the total amount of the accreted ice structures to be removed for the anti-/de-icing operation.

Fig. 6(a) shows the dynamic ice accretion process over the hydrophilic surface of the turbine blade model without any ant-/de-icing measures (i.e., the baseline HPS case) under the glaze icing condition (i.e., $V_\infty = 40$ m/s; $T_\infty = -5$ °C; $LWC = 2.0$ g/m^3). It can be seen clearly that, after the super-cooled water droplets carried by the incoming airflow impinged onto the surface of the turbine blade model (i.e., mainly in the region near the leading edge of the blade model), only a portion of the impacted water droplets were found to be frozen into ice. The remaining portion of the impacted water mass was found to form a thin water film flow at first, and then run back as driven by the boundary layer airflow over the iced surface of the turbine blade model. The water film flow was found to split into multiple rivulets as running back and was found to be frozen into ice subsequently at further downstream locations. As time goes by, more and more supercooled water droplets would impact onto the turbine model surface. Therefore, the ice structures accreted over the turbine blade model were found to become larger and larger with a transparent appearance, i.e., a typical feature of glaze ice accretion. Finally, the entire surface of the blade model was found to be covered with complicated glaze ice structures as the ice accretion time increase long enough.

In comparison to the ice accretion process over the hydrophilic blade model surface (i.e., HPS case), much less ice accretion was found over the SHS-coated blade model surface (i.e., SHS cases), as shown clearly in Fig. 5(b). The accreted ice structures were found to mainly concentrate in the region near the blade leading edge, instead of covering a much greater area over the hydrophilic blade model. Similar as that reported in Liu et al. [57], the unfrozen surface water was found to be able to run back much faster over the SHS coated blade surface, and more readily to shed or roll off from the SHS-coated blade model. As a result, no ice structures were found to accrete over the rear portion of SHS-coated blade mode model, similar to that described in Mangini et al. [49]. It is suggested that there are two main reasons for the faster surface water runback over the SHS-coated blade surface: 1) with the same incoming freestream airflow velocity, in corresponding to the much greater contact angles and smaller wet area for the impacted water droplets/rivulets over the SHS-coated surface, the aerodynamic shear forces acting on the water droplets/rivulets over the SHS-coated surface would also become much greater. 2) even for the scenario as driven by the same aerodynamic shear force, the much less resistance due to the smaller capillary force and weaker ice adhesion strength would enable a much faster moving speed of the runback water/ice mixtures over the SHS-coated blade surface (i.e., SHS case) in comparison to that over the hydrophilic blade surface (i.e., HPS case).

It should also be noted that, since the aerodynamic shear forces in the region near the airfoil leading edge would become very small and even can be vanished at the stagnation line, they would be too weak to overcome the capillary force or/and ice adhesion strength, even over the SHS-coated blade surface. As a result, once the first

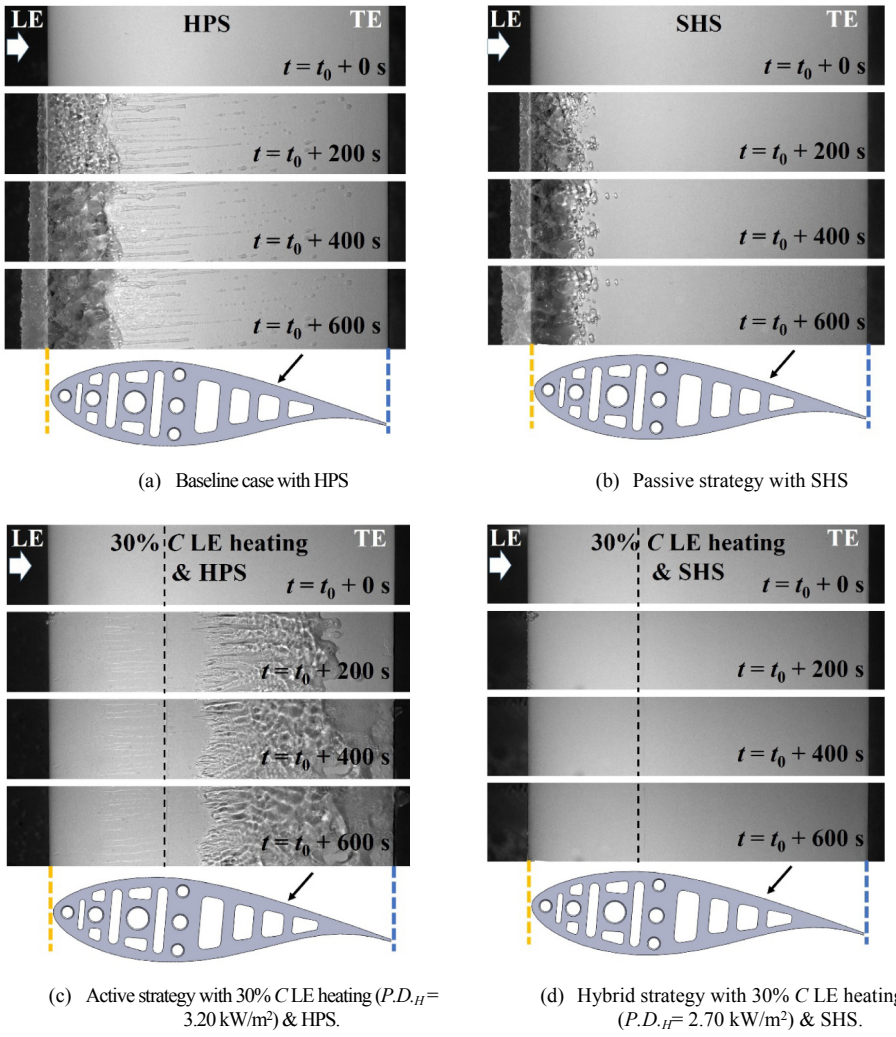

(a) Baseline case with HPS

(b) Passive strategy with SHS

(c) Active strategy with 30% *C* LE heating ($P.D._H$ = 3.20 kW/m^2) & HPS.

(d) Hybrid strategy with 30% *C* LE heating ($P.D._H$ = 2.70 kW/m^2) & SHS.

Fig. 6. Comparison of various anti-/de-icing strategies under the typical glaze icing condition.

ice features were found to accrete in the region near the stagnation line of the turbine blade model, the subsequent super-cooled water droplets would impact onto the surface of the accreted ice, instead of SHS-coated blade surface, which would accelerate the ice accretion process in the region near the blade leading edge tremendously. Therefore, as shown clearly in Fig. 6(b), while the passive strategy with SHS coating was found to be able to reduce ice accretion over the SHS-coated blade surface significantly (i.e., ice accretion area was found reduced greatly from majority of the blade surface to a much narrower region near the leading edge), it is still far from sufficient to successfully prevent ice formation/accretion over the entire surface of the turbine blade model.

As shown clearly in Fig. 6(c), the active strategy with 30%*C* LE heating was found to be very effective to eliminate ice formation/accretion in the region near the blade leading edge. It should be noted that, the input power density supplied to LE heating element for the present 30%*C* LE heating strategy was set to be 3.20 kW/m^2, i.e., as the same value as the case with the entire surface heating strategy (i.e., 100% *C* heating) described above. It reveals clearly that, with the 30%*C* LE heating strategy, the region near the blade leading edge was found be completely ice-free, as expected. It indicates that the heat fluxes provided by the electric heating element wrapped around the blade leading edge is sufficient to heat up the impinged super-cooled water droplets and make them be in the liquid phase over the heated blade surface. However, as running back to reach further downstream regions, the impacted surface water could not always stay in the liquid phase over the blade surface. As shown clearly in Fig. 6(c), when the surface water moved to further downstream region beyond the area protected by the electric heating element, the runback surface water was found to be frozen into ice eventually, i.e., forming runback ice in the downstream region at the rear surface of the turbine blade model. The irregular-shaped ice structures accreted over the rear surface of the turbine blade model would cause severe negative effects on the aerodynamic and structural performances of the turbine blades. In summary, by using the LE heating strategy only, it was also failing to keep the entire surface of the turbine blade model ice-free.

Fig. 6(d) shows the anti-/de-icing performance of the hybrid strategy that combines both the LE heating and SHS coating for wind turbine icing mitigation. During the entire 10-min duration of the glaze icing experiment, the entire blade model was found to be completely free of ice, showing an outstanding anti-/de-icing performance. For the test case given in Fig. 6(d), the minimum power density supplied for the electric heating element was set to be 2.70 kW/m^2, which is even smaller than that required value for the 30% LE heating strategy. This is believed to be due to the fact that the effective rebounding of the impacted super-cooled water droplets from the SHS coated blade surface would result in much

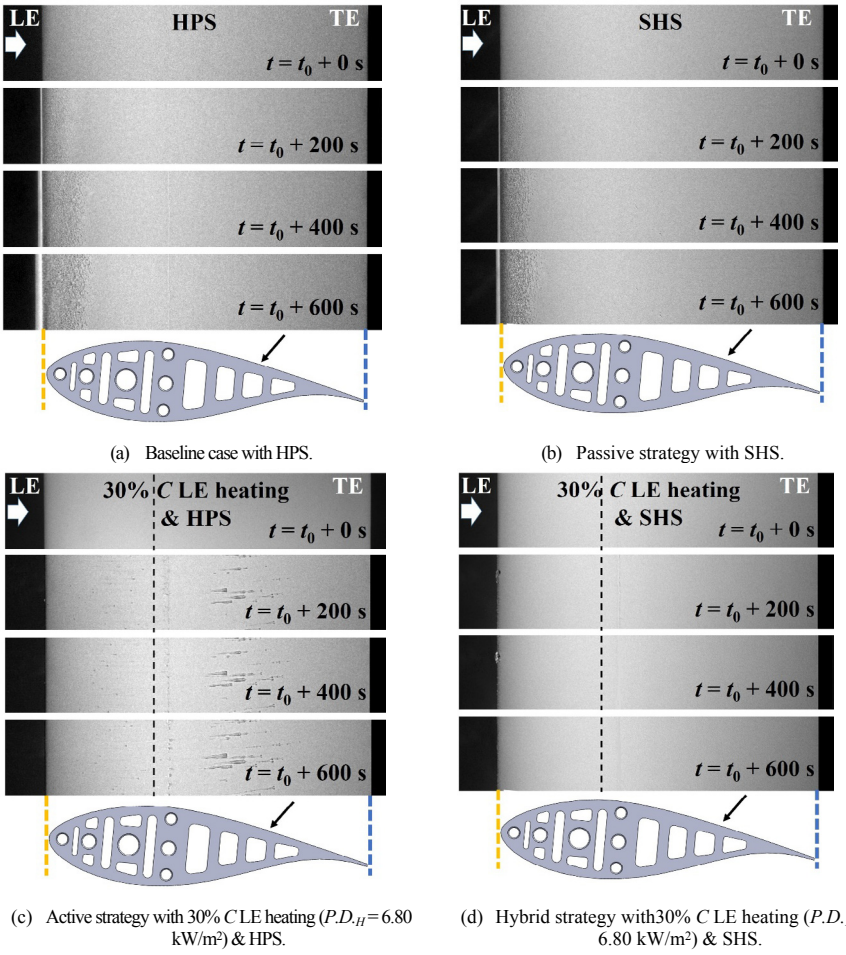

(a) Baseline case with HPS.

(b) Passive strategy with SHS.

(c) Active strategy with 30% *C* LE heating ($P.D._H = 6.80$ kW/m²) & HPS.

(d) Hybrid strategy with30% *C* LE heating ($P.D._H = 6.80$ kW/m²) & SHS.

Fig. 7. Comparison of various anti-/de-icing strategies under the typical rime icing condition.

less amount of the impacted water mass remaining on the SHS coated blade surface for possible ice formation/accretion.

Fig. 7 gives the experimental results to demonstrate the effectiveness of various anti-/de-icing strategies under the typical rime icing condition of $V_\infty = 40$ m/s, $T_\infty = -10$ °C, $LWC = 0.4$ g/m^3, which reveal very similar features in the anti-/de-icing operation of the investigated strategies described above. As shown in Fig. 7(a), under such a rime icing condition (i.e., much colder ambient temperature and lower LWC level), the super-cooled water droplets were found to be frozen immediately upon impacting onto the hydrophilic blade surface and start to form ice structures with opaque milk-white appearance and tiny grain size instantly. Since the impingement of the super-cooled water droplets carried by the incoming airflow concentrate mainly within a narrow region near the blade leading edge (i.e., mainly within the impinging limit as describe in Liu et al. [61]), the ice structures were found to accrete mainly in the region near the blade leading edge. No runback ice accretion was observed over the surface of the blade model under the rime icing condition, as expected.

In comparison to the ice structures accreted over the conventional hydrophilic surface of the turbine blade model, a marginal better anti-/de-icing capability was observed for the passive strategy with the SHS coating to cover the blade model surface. As revealed clearly in Fig. 7(b), the thickness of the ice layer as well as the ice accretion area near the blade leading edge were found to be much smaller over the SHS-coated blade surface, in comparison to those over the hydrophilic blade surface. As shown clearly in Fig. 4(b), since the impacted super-cooled water droplets would be more readily to be bouncing off from impacted SHS, a small portion of the impacted water mass would remain on the SHS-coated blade surface for ice accretion.

Fig. 7(c) shows the acquired snapshot images for the active anti-/de-icing strategy case with 30% *C* LE heating. It can be seen clearly that, with a power input of 6.80 kW/m^2 supplied to the electric heating element wrapped around the blade leading edge, the impacted super-cooled water droplets were found to be heated up effectively to remain in liquid phase after impinging onto the heated blade surface. As driven by the airflow over the heated blade surface, the water mass collected at the blade leading edge would run back rapidly, moving to further downstream locations on the hydrophilic blade surface. Since the electric heating element covers only the first 30% of the blade surface for this case, the runback water was found to be frozen into ice in the further downstream region beyond the area protected by the electric heating element. Therefore, runback ice accretion was observed to occur over the hydrophilic surface of the turbine blade model, i.e., at ~50% chord length downstream, as shown clearly in Fig. 7(c).

Fig. 7(d) shows the acquired snapshot images of the case with the hybrid anti-/de-icing strategy (i.e., combining 30% LE heating with SHS). It can be seen clearly that, the hybrid anti-/de-icing strategy was very successful again in preventing ice formation/accretion over the entire surface of the turbine blade model under the rime icing condition. As shown in Fig. 4(b), after impinging onto the SHS coated blade surface, the water droplets would break down

into many smaller droplets with the majority of the impacted water mass bouncing off from the SHS-coated blade surface. The remaining portion of the impacted water would be either evaporated directly over the heated blade surface or run back very fast, and eventually shedding/rolling off from the surface of the turbine blade model swiftly before being frozen into ice. As a result, no ice formation/accretion was observed over the entire SHS coated blade surface during the entire 10-min duration of the icing experiment. In summary, the experimental results given above demonstrate clearly that, the hybrid ant-/de-icing strategy would successfully prevent ice formation/accretion over the entire surface of the turbine blade model under both the glaze and rime icing conditions.

4.3. Measured surface temperature distributions during the anti-/de-icing operation

Fig. 8 shows the time evolutions of the measured temperature distributions on the surface of the turbine blade model during the anti-/de-icing operations with the 30% C LE heating strategy (i.e., blade surface still being hydrophilic) and the hybrid anti-/de-icing strategy (30%C LE heating and SHS) under the typical glaze icing condition (i.e., $V_\infty = 40$ m/s, $T_\infty = -5$ °C and LWC = 2.0 g/m^3). During the experiments, the same power input was supplied to the electric heating elements for the two compared cases. The time evolutions of the measured surface temperature variations (i.e., $\Delta T = T - T_\infty$) at four typical down locations, i.e., at X/C = 0.05, 0.10, 0.15 and 0.25 over the turbine blade model were also given in Fig. 8 for a quantitative comparison.

After the electric heating element wrapped around the blade leading edge was switched on, the surface temperature in the region near the blade leading edge was found to increase monotonically at first, then reached a relatively stable state with the surface temperature of the heated blade surface being greater than the water frozen temperature (i.e., $T > 0$ °C). As shown clearly in Fig. 8, the surface temperature at the rear portion of the heated blade surface was found to much higher than those in near blade leading edge due to the much stronger conductive heat transfer process near the airfoil leading edge, as described in Liu and Hu [61]. The surface temperature in the downstream region right beyond the heated area was also found to increase slightly due to both the heat conduction via the substrate of the blade model and the heat convection via the boundary layer airflow over the surface of the turbine blade model.

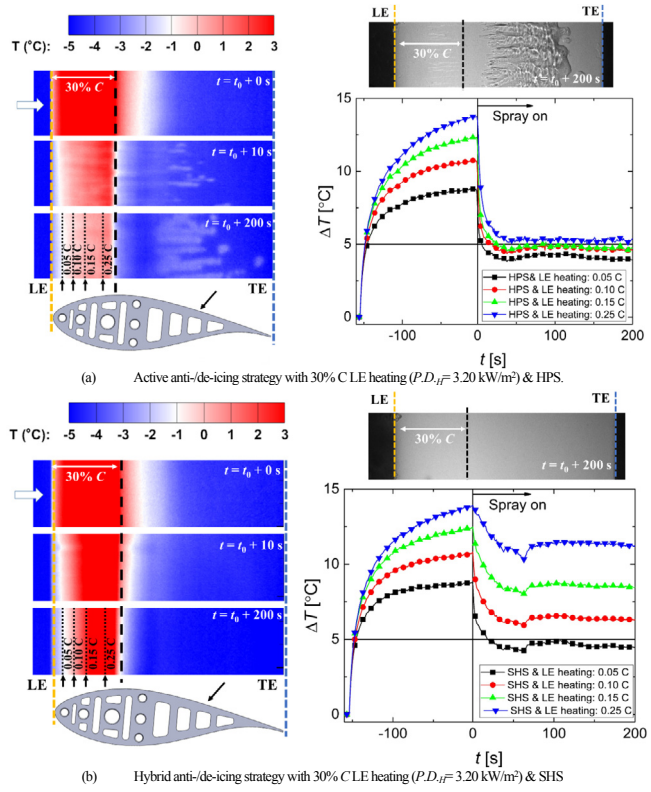

Fig. 8. Time evolutions of temperature distribution over the surface of the turbine blade model under the typical glaze icing condition ($V_\infty = 40$ m/s, $T_\infty = -5$ °C and LWC = 2.0 g/m^3).

After the electric heating element reaching the thermal steady state at the time of $t = t_0$, the water spray system of ISU-IRT was switched to start the anti-/de-icing experiment. As revealed clearly from the IR thermal imaging results given in Fig. 8, upon the impacting of the super-cooled water droplets onto the turbine blade model, the surface temperature of the heated surface near the blade leading edge was found to drop dramatically at first, and then reached a stable state eventually. For the test case with the blade surface being hydrophilic, the temperature of the heated surface near the blade leading edge was found to stay slightly above the water frozen temperature (i.e., $\Delta T = T - T_\infty \approx 5.0$ °C), as shown clearly in Fig. 8(a). It indicates that, after impinged onto the heated blade surface, the super-cooled water droplets (i.e., with their original temperature being $T_\infty = -5$ °C) would be heated up rapidly and stayed in the liquid phase. The impacted surface water would run back, as driven by the boundary layer airflow over the surface or the blade model. Since the ambient temperature was kept at a frozen-cold temperature of $T_\infty = -5.0$ °C during the anti-/de-icing experiment, the runback water was found to be re-frozen into ice at further downstream locations of the hydrophilic blade surface, as revealed clearly in the acquired snapshot image given in Fig. 8(a). It can also be seen that, the refreezing of the runback surface water at the downstream locations beyond the area protected by the electric heating element would lead to a slight temperature increase due to the release of the latent heat of fusion during the solidification of the runback water [69].

As shown clearly in Fig. 8(b), for the test case of the hybrid anti-/de-icing strategy, the characteristics of the temperature variations over the SHS-coated blade surface were found to become quite different in comparison to those with the blade model surface being hydrophilic. Since the same power input was supplied to the electric heating element for the two compared cases, the temperature increase over the heated surface in the region near the blade leading edge was found to be quite similar before switching on the water spray system of ISU-IRT to start the ice accretion process, as expected. However, after switching on the water spray system of ISU-IRT to start the ice accretion process, the temperature variations over the SHS-coated blade surface for the hybrid anti-/de-icing strategy case were found to become significantly different those of the test case with hydrophilic blade surface. Since a significant portion of the impacted super-cooled water droplets would be bouncing off from the SHS-coated blade surface as shown in Fig. 4(b), much less amount of the impacted water mass would remain on the SHS-coated blade surface. Since the same amount of the power input was supplied to the electric heating element for the two compared cases, the much less impacted water mass to be heated by the electric heating element over the SHS-coated blade surface would result in a much higher surface temperature of the heated blade surface. As shown, clearly in Fig. 8 (b), since the impacted surface water was heated up to a much higher temperature, it would be much more unlikely to be frozen into ice as running back over the SHS-coated blade surface. Furthermore, since the moving speed of the runback water would be much

higher over the SHS-coated blade surface due to the much smaller capillary force, the impacted surface water would be much more readily to shed/roll off from the surface of the turbine blade model before forming runback ice. Therefore, as shown clearly in the snapshot image given Fig. 8(b), no ice was observed to over the SHS-coated blade surface for the case with the hybrid anti-/de-icing strategy.

4.4. A parametric study to explore/optimize the design paradigm of the hybrid anti-/de-icing strategy

As described above, for the hybrid anti-/de-icing strategy with the electric heating element covering the front 30% of the blade surface, the impacted water droplets over the SHS-coated blade surface would be heated up to a much higher temperature, i.e., well above the water -freezing temperature to prevent ice formation/accretion. While it was found to be able to keep the entire blade model surface ice-free, a portion of the power input supplied to the electric heating element may be wasted due to the overheating of the impacted supper-cooled water droplets. Therefore, a parametric study was also performed to explore/optimize the design paradigm of the hybrid anti-icing strategy to minimize the required power input for the anti-/deicing operation. In the parametric study, the size of the electric heating film wrapped around blade leading edge was changed to cover 5%, 10%, 30% and 100% of the blade surface, respectively. For the first three test cases (i.e., with the area coverage of the heated area being 5%, 10% and 30% of the blade surface), both the surface of the electric heating element and the rest of the unheated blade surface were all coated with the SHS coating. For the test case with the electric heating element covering the entire blade surface (i.e., 100% heating case), the surface of the blade model (i.e., the upper surface of the electric heating element) was set to be hydrophilic to be the same as a typical conventional wind turbine blade, which was used as the baseline for the comparative study.

By following the same experimental procedure as that described above, the minimum power inputs needed for a successful anti-icing operation (i.e., to keep the entire blade surface ice-free) with coverage of the electric heating elements were determined under the typical glaze icing condition (i.e., $V_\infty = 40$ m/s, LWC $= 2.0$ g/m^3, and $T_\infty = -5$ °C) and rime icing condition (i.e., $V_\infty = 40$ m/s, LWC $= 0.4$ g/m^3, and $T_\infty = -10$ °C). Fig. 9 shows typical snapshot images for the hybrid anti-/de-icing strategy with the electric heating element covering only 5% of the blade front surface, which reveal some interesting features in using the hybrid strategy for anti-/de-icing operation. As described above, the super-cooled water droplets would be heated up rapidly after impacted onto the heated blade surface (i.e., mainly within the airfoil impinging limit near the airfoil leading edge as described in Liu and Hu [61]). When an adequate power input of $P.D._H = 7.80$ kW/m^2 was supplied to the electric heating element wrapped around the blade leading edge, the temperature of the impacted surface water over the SHS-coated surface would increase to a level much higher than the water freezing temperature. The "warmed" water would run back very rapidly over the SHS-coated blade surface and shedding subsequently from the trailing edge of the blade model before forming runback ice. As a result, the SHS-coated blade surface was found to be completely ice-free, as shown clearly in Fig. 9(a).

However, when the power input supplied to the electric heating element was not high enough, e.g., $P.D._H = 5.30$ kW/m^2 only as shown in Fig. 9(b), while the super-cooled water droplets would be heated up and stay in the liquid phase after impacted onto the heated blade surface near the leading edge, the runback surface water was found to be refrozen into ice, i.e., to form runback ice, in the downstream region beyond the area protected by the electric heating element. Once the ice was found to accrete over the surface of the blade model, subsequent runback water would accumulate rapidly over the surface of the accreted ice to promote much faster growth of the accreted ice structures, as shown clearly in Fig. 9(a) at $t = t_0 + 200$ s. As the size of the accreted ice structures increases, the aerodynamic shear force acting on the ice structures accreted over the SHS-coated blade surface would become greater and greater. The aerodynamic forces acting on the ice structures would become strong enough to overcome the ice adhesion strength over the SHS-coated blade surface eventually. As a result, the large ice chunk would shed/roll off from the SHS-coated blade surface, as shown clearly in Fig. 9(a) at $t = t_0 + 409$ s. As time goes on, another cycle of the ice accretion process was found to occur, which

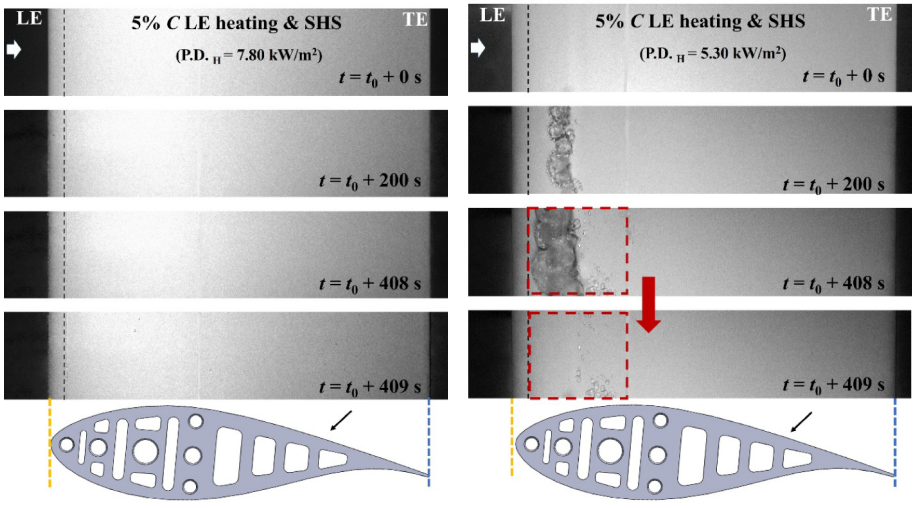

(a). at $P.D._H = 7.80$ kW/m^2 (b). at $P.D._H = 5.30$ kW/m^2

Fig. 9. Snapshot images to reveal the anti-/de-icing operation of the hybrid strategies with only 5% *C* LE heating under the glaze icing condition of $V_\infty = 40$ m/s, $T_\infty = -5$ °C, LWC $= 2.0$ g/m^3. The red dash squares highlight the ice shedding over the blade surface.

repeated the process as described above.

In the present study, a parameter named required total power density (i.e., $P.D._{total}$) was introduced in order to provide a quantitative comparison of the required power consumption for all the test cases, which was defined as:

$$P.D._{total} = \frac{P.D._H \times L_H}{C} \tag{3}$$

where L_H is the chord-wise length of the heated area over the turbine blade model, i.e., $L_H = 100\%C$, 30% C, 10% C and 5% C, respectively for the test cases compared in the present study.

Furthermore, in order to demonstrate the advantage of the hybrid anti-/de-icing strategy over the conventional brutally-heating strategy (i.e., 100% surface heating), the saving in the required power consumption *(i.e., Power-Saving)* by using the hybrid strategy for a successful anti-/de-icing operation is calculated with the following equation:

$$Power - Saving = \left(\left(P.D._{total} - P.D._{total,ref}\right)\Big/ P.D._{total,ref}\right) \times 100\%, \tag{4}$$

where $P.D._{total,ref}$ is the minimum required $P.D._{total}$ of the reference case with the entire blade surface heated by the electric heating element (i.e., 100% C heating case).

Table 2 summarizes the results of the parametric study for a quantitative comparison of all the test cases under both the glaze icing and rime icing conditions. It can be seen clearly that, in comparison to the conventional brutally heating strategy (i.e., 100% surface heating case), the hybrid anti-/de-icing strategy with a minimized LE heating coverage and the SHS coating would achieve a maximum power saving of 90% and 94% under the glaze icing and rime icing conditions, respectively. It indicates that, in comparison to the conventional brutally heating strategy, the hybrid anti-/de-icing strategy (i.e., by combining the minimized surface heating near the blade leading edge and the SHS-coating) would only consume only ~10% power input to reach the same ant-/de-icing performance to keep the entire blade surface ice-free. The significant power saving by using the hybrid anti-/de-icing strategy would ensure most of the electricity generated by wind turbines to be integrated into the power grid, instead of being consumed locally to heat the blade surfaces for anti-/de-icing operation.

5. Conclusions

In the present study, a hybrid anti-/de-icing strategy that combines the minimized surface heating near the blade leading edge and using a superhydrophobic surface (SHS) coating to cover the entire turbine blade surface was explored for wind turbine icing mitigation. The experimental study was conducted in the unique Icing Research Tunnel available at Iowa State University (i.e., ISU-IRT), which was used to generate a wet glaze icing condition (i.e., $V_\infty = 40$ m/s, $T_\infty = -5\,^\circ$C, LWC $= 2.0$ g/m^3) and a dry rime icing condition (i.e., $V_\infty = 40$ m/s, $T_\infty = -10\,^\circ$C, and LWC $= 0.4$ g/m^3) to be representative of the typical icing conditions experienced by wind turbines in cold weathers. A turbine blade/airfoil model with DU91-W2-250 airfoil profile in the cross section was manufactured and mounted in the test section of ISU-IRT to evaluate the effectiveness of various anti-/de-icing strategies. The test cases compared in the present study include: 1). the blade model with hydrophilic surface (i.e., HPS case in short) as the comparison baseline to represent conventional wind turbine blade without any icing protection measures; 2). A passive anti-/de-icing strategy to have the turbine blade model coated with a super-hydrophobic surface (SHS) coating (i.e., SHS case in short); 3). An active anti-/de-icing strategy with a thin electric heating film to wrap around the leading edge (LE) (of the turbine blade model and keep the entire turbine model surface still being hydrophilic as the baseline case (i.e., LE heating case in short); and 4). A hybrid anti-/de-icing strategy combining the surface heating at the blade leading edge and using a SHS coating to cover the entire blade surface (i.e., the hybrid case in short). During the experiment, while a high-speed imaging system was utilized to reveal the dynamic ice accretion process over the surface of the turbine blade model under different icing conditions, a high-speed infrared (IR) thermal imaging system was also used to quantify the time evolutions of the temperature distributions over the surface of the turbine blade model during the anti-/de-icing operations with different anti-/de-icing strategies.

It was found that, in comparison with the baseline case with the turbine blade model be hydrophilic (i.e., HPS case), the ice accretion area over the SHS coated blade surface was found to be reduced substantially due to the much faster runback speed of the impacted surface water and the weaker ice accretion strength over the SHS coated blade surface. However, ice accretion was still found to occur in the region near the blade leading edge due to the much weaker aerodynamic shear forces in the region near the stagnation line of the turbine blade model. It indicates that, it is impossible to keep the entire blade surface ice-free by using only the passive anti-/de-icing strategy with SHS coatings. While the LE heating strategy was found to be effective to heat up the impacted super-cooled water droplets to stay in liquid phase, thereby, preventing ice formation/accretion in the region near the blade leading edge (i.e., within the area protected by the electric heating element). However, as running back over the hydrophilic blade surface, the surface water was found to be re-frozen into ice subsequently (i.e., to start runback icing) in the downstream region beyond the area protected by the electric heating element. As a result, the entire blade surface would need to be heated (i.e., 100% surface heating case) in order to ensure the entire blade surface ice-free.

By combining the passive strategy with SHS coating to eliminate the runback icing and the active strategy with a minimized surface heating to prevent ice formation near the blade leading edge, the hybrid strategy was found to be capable of keeping the entire blade surface completely ice-free under both wet glaze icing and dry rime icing conditions. A parametric study was performed to explored/optimize the design paradigms of the hybrid anti-/de-icing strategy

Table 2
Measurement Results of the parametric study under both the glaze and rime icing condition.

Strategy	Glaze icing condition $V_\infty = 40$ m/s, $T_\infty = -5\,^\circ$C, and LWC $= 2.0$ g/m^3				Rime icing condition $V_\infty = 40$ m/s, $T_\infty = -10\,^\circ$C, and LWC $= 0.4$ g/m^3			
	$P.D._H$ [kW/m^2]	$P.D._{total}$ [kW/m^2]	Power Saving	Note	$P.D._H$ [kW/m^2]	$P.D._{total}$ [kW/m^2]	Power Saving	Note
100% C heating & HPS (baseline)	3.20	3.20	0	Ice free	6.80	6.80	0	Ice free
30% C LE heating & SHS	2.70	0.81	74%	Ice free	6.80	0.81	74%	Ice free
10% C LE heating & SHS	3.20	0.32	90%	Ice free	6.80	0.68	90%	Ice free
5% C LE heating & SHS	7.80	0.39	88%	Ice free	7.80	0.39	94%	Ice free

in order to minimize the required power input for the anti-/deicing operation. By using the SHS coating to cover the entire blade surface, the hybrid strategy with the electric heating element covering only 5%–10% of the blade front surface was found to have the optimal anti-/de-icing performance (i.e., minimized required power consumption for a successful anti-/de-icing operation). It was demonstrated that, instead of using the conventional strategy to brutally heat the entire hydrophilic blade surface, the optimized hybrid strategy can keep the entire blade surface ice-free with only ~10% of the required power consumption, making hybrid strategy a very promising anti-/de-icing method to ensure the safer and more efficient operation of wind turbines in cold weathers.

Conflicts of interest

The authors declare no conflict of interest.

Acknowledgments

This research was supported by National Science Foundation (NSF) under award numbers of OISE-1826978 and CMMI-1824840. The authors would like to thank Dr. Rye Waldman and Mr. Prashanth Beeram for their contributions in ice adhesion strength measurements.

References

[1] A. Chehouri, R. Younes, A. Ilinca, J. Perron, Review of performance optimization techniques applied to wind turbines, Appl. Energy 142 (2015) 361–388, https://doi.org/10.1016/j.apenergy.2014.12.043.
[2] BP, BP Statistical Review of World Energy 2017, Br Pet 2017:1–52, http://www.bp.com/content/dam/bp/en/corporate/pdf/energy-economics/statistical-review-2017/bp-statistical-review-of-world-energy-2017-full-report.pdf.
[3] V. Lehtomäki, Wind Energy in Cold Climates Available Technologies - Report, 2016.
[4] F. Lamraoui, G. Fortin, R. Benoit, J. Perron, C. Masson, Atmospheric icing impact on wind turbine production, Cold Reg. Sci. Technol. 100 (2014) 36–49, https://doi.org/10.1016/j.coldregions.2013.12.008.
[5] F. Feng, S. Li, Y. Li, W. Tian, Numerical simulation on the aerodynamic effects of blade icing on small scale Straight-bladed VAWT, Phys Procedia 24 (2012) 774–780, https://doi.org/10.1016/j.phpro.2012.02.115.
[6] S. Barber, Y. Wang, S. Jafari, N. Chokani, R. Abhari, The Impact of Ice Formation on Wind Turbine Performance and Aerodynamics, ASME. J. Sol. Energy Eng. 133 (1) (2011), https://doi.org/10.1115/1.4003187, 011007-011007-9.
[7] W. Shi, X. Tan, Z. Gao, T. Moan, Numerical study of ice-induced loads and responses of a monopile-type offshore wind turbine in parked and operating conditions, Cold Reg. Sci. Technol. 123 (2016) 121–139, https://doi.org/10.1016/j.coldregions.2015.12.007.
[8] B. Lu, Y. Li, X. Wu, Z. Yang, A review of recent advances in wind turbine condition monitoring and fault diagnosis, in: IEEE Conf Power Electron Mach Wind Appl, 2009, pp. 1–7, https://doi.org/10.1109/PEMWA.2009.5208325.
[9] Colin Morgan, E. Bossany, H. Seifert, Assessment of Safety Risks arising from Wind Turbine Icing, Boreas VI - Wind Energy Prod Cold Clim, 1998, 113–21.
[10] Q. Liu, Y. Yang, M. Huang, Y. Zhou, Y. Liu, X. Liang, Durability of a lubricant-infused Electrospray Silicon Rubber surface as an anti-icing coating, Appl. Surf. Sci. 346 (2015) 68–76, https://doi.org/10.1016/j.apsusc.2015.02.051.
[11] O. Parent, A. Ilinca, Anti-icing and de-icing techniques for wind turbines: critical review, Cold Reg. Sci. Technol. 65 (2011) 88–96, https://doi.org/10.1016/j.coldregions.2010.01.005.
[12] O. Fakorede, H. Ibrahim, A. Ilinca, J. Perron, Experimental investigation of power requirements for wind turbines electrothermal anti-icing systems, Wind Turbines Des. Control Appl. (2016), https://doi.org/10.5772/63449.
[13] O. Fakorede, Z. Feger, H. Ibrahim, A. Ilinca, J. Perron, C. Masson, Ice protection systems for wind turbines in cold climate: characteristics, comparisons and analysis, Renew. Sustain. Energy Rev. 65 (2016) 662–675, https://doi.org/10.1016/j.rser.2016.06.080.
[14] M. Pourbagian, W.G. Habashi, Aero-thermal optimization of in-flight electro-thermal ice protection systems in transient de-icing mode, Int. J. Heat Fluid Flow 54 (2015) 167–182, https://doi.org/10.1016/j.ijheatfluidflow.2015.05.012.
[15] L. Battisti, Wind Turbines in Cold Climates, 2015, https://doi.org/10.1007/978-3-319-05191-8.
[16] H. Seifert, Technical requirements for rotor blades operating in cold climate, Proc. Boreas VI 50–5 (2003).
[17] W. Yu, J. Tao, X. Yu, S. Zhao, S.T. Tu, H. Liu, A microreactor with superhydrophobic Pt–Al2O3catalyst coating concerning oxidation of hydrogen off-gas from fuel cell, Appl. Energy 185 (2017) 1233–1244, https://doi.org/10.1016/j.apenergy.2016.01.048.
[18] Z. Hong, H. Yang, W. Yuanhao, Y. Hongxing, TiO2/Silane coupling agent composed two layers structure: a novel stability super-hydrophilic self-cleaning coating applied in PV panels, Energy Procedia 105 (2017) 1077–1083, https://doi.org/10.1016/j.egypro.2017.03.464.
[19] A.G. Kraj, E.L. Bibeau, Phases of icing on wind turbine blades characterized by ice accumulation, Renew. Energy 35 (2010) 966–972, https://doi.org/10.1016/j.renene.2009.09.013.
[20] Z.J. Wang, D.J. Kwon, K. Lawrence DeVries, J.M. Park, Frost formation and anti-icing performance of a hydrophobic coating on aluminum, Exp. Therm. Fluid Sci. 60 (2015) 132–137, https://doi.org/10.1016/j.expthermflusci.2014.09.003.
[21] C. Peng, S. Xing, Z. Yuan, J. Xiao, C. Wang, J. Zeng, Preparation and anti-icing of superhydrophobic PVDF coating on a wind turbine blade, Appl. Surf. Sci. 259 (2012) 764–768, https://doi.org/10.1016/j.apsusc.2012.07.118.
[22] A. Lopera-Valle, A. McDonald, Flame-sprayed coatings as de-icing elements for fiber-reinforced polymer composite structures: modeling and experimentation, Int. J. Heat Mass Transf. 97 (2016) 56–65, https://doi.org/10.1016/j.ijheatmasstransfer.2016.01.079.
[23] F. Arianpour, M. Farzaneh, S.A. Kulinich, Hydrophobic and ice-retarding properties of doped silicone rubber coatings, Appl. Surf. Sci. 265 (2013) 546–552, https://doi.org/10.1016/j.apsusc.2012.11.042.
[24] J.M. Pinar Pérez, F.P. García Márquez, D. Ruiz Hernández, Economic viability analysis for icing blades detection in wind turbines, J. Clean. Prod. 135 (2016) 1150–1160, https://doi.org/10.1016/j.jclepro.2016.07.026.
[25] I. Baring-Gould, L. Tallhaug, G. Ronsten, R. Horbaty, R. Cattin, T. Laakso, et al., Expert Group Study on Recommendations for Wind Energy Projects in Cold Climates, 2009.
[26] H. Yan, W. Yuanhao, Y. Hongxing, TEOS/silane coupling agent composed double layers structure: a novel super-hydrophilic coating with controllable water contact angle value, Appl. Energy 185 (2017) 2209–2216, https://doi.org/10.1016/j.apenergy.2015.09.097.
[27] C. Mayer, A. Ilinca, G. Fortin, J. Perron, Wind tunnel study of electro-thermal de-icing of wind turbine blades, Int. J. Offshore Polar Eng. 17 (2007).
[28] W. Zhou, Y. Liu, H. Hu, H. Hu, X. Meng, Utilization of thermal effect induced by plasma generation for aircraft icing mitigation, AIAA J. 56 (2018) 1–8, https://doi.org/10.2514/1.J056358.
[29] Y. Liu, C. Kolbakir, H. Hu, H. Hu, A comparison study on the thermal effects in DBD plasma actuation and electrical heating for aircraft icing mitigation, Int. J. Heat Mass Transf. 124 (2018) 319–330, https://doi.org/10.1016/J.IJHEATMASSTRANSFER.2018.03.076.
[30] C. Yin, Z. Zhang, Z. Wang, H. Guo, Numerical simulation and experimental validation of ultrasonic de-icing system for wind turbine blade, Appl. Acoust. 114 (2016) 19–26, https://doi.org/10.1016/j.apacoust.2016.07.004.
[31] H. Habibi, G. Edwards, C. Sannassy, V. Kappatos, Y. Lage, J. Stein, et al., Modelling and empirical development of an anti/de-icing approach for wind turbine blades through superposition of different types of vibration, Cold Reg. Sci. Technol. 128 (2016) 1–12, https://doi.org/10.1016/j.coldregions.2016.04.012.
[32] L. Gao, Y. Liu, H. Hu, An experimental investigation on the dynamic ice accretion process over the surface of a wind turbine blade model, in: 9th AIAA Atmos. Sp. Environ. Conf, American Institute of Aeronautics and Astronautics, Reston, Virginia, 2017, https://doi.org/10.2514/6.2017-3582.
[33] L. Gao, Y. Liu, W. Zhou, H. Hu, An experimental study on the aerodynamic performance degradation of a wind turbine blade model induced by ice accretion process, Renew. Energy 133 (2019) 663–675, https://doi.org/10.1016/J.RENENE.2018.10.032.
[34] A. Albers, Summary of a Technical Validation of ENERCON 's Rotor Blade De-icing System, 2011 doi:PP11035.
[35] P. Zhang, F.Y. Lv, A review of the recent advances in superhydrophobic surfaces and the emerging energy-related applications, Energy 82 (2015) 1068–1087, https://doi.org/10.1016/j.energy.2015.01.061.
[36] L. Cao, A.K. Jones, V.K. Sikka, J. Wu, D. Gao, Anti-icing superhydrophobic coatings, Langmuir 25 (2009) 12444–12448, https://doi.org/10.1021/la902882b.
[37] P. Tourkine, M. Le Merrer, D. Quéré, Delayed freezing on water repellent materials, Langmuir 25 (2009) 7214–7216, https://doi.org/10.1021/la900929u.
[38] C. Antonini, M. Innocenti, T. Horn, M. Marengo, A. Amirfazli, Understanding the effect of superhydrophobic coatings on energy reduction in anti-icing systems, Cold Reg. Sci. Technol. 67 (2011) 58–67, https://doi.org/10.1016/j.coldregions.2011.02.006.
[39] Z. Zhang, B. Chen, C. Lu, H. Wu, H. Wu, S. Jiang, et al., A novel thermo-mechanical anti-icing/de-icing system using bi-stable laminate composite structures with superhydrophobic surface, Compos. Struct. 180 (2017) 933–943, https://doi.org/10.1016/j.compstruct.2017.08.068.
[40] K.R. Khedir, G.K. Kannarpady, C. Ryerson, A.S. Biris, An outlook on tunable superhydrophobic nanostructural surfaces and their possible impact on ice mitigation, Prog. Org. Coating 112 (2017) 304–318, https://doi.org/10.1016/j.porgcoat.2017.05.019.
[41] M. Ruan, W. Li, B. Wang, B. Deng, F. Ma, Z. Yu, Preparation and anti-icing behavior of superhydrophobic surfaces on aluminum alloy substrates, Langmuir 29 (2013) 8482–8491, https://doi.org/10.1021/la400979d.

[42] S. Zhang, J. Huang, Y. Cheng, H. Yang, Z. Chen, Y. Lai, Bioinspired surfaces with superwettability for anti-icing and ice-phobic application: concept, mechanism, and design, Small (2017), https://doi.org/10.1002/smll.201701867, 1701867:1701867.
[43] P. Kim, T.-S. Wong, J. Alvarenga, M.J. Kreder, W.E. Adorno-Martinez, J. Aizenberg, Liquid-infused nanostructured surfaces with extreme anti-ice and anti-frost performance, ACS Nano 6 (2012) 6569–6577, https://doi.org/10.1021/nn302310q.
[44] Y. Wang, J. Xue, Q. Wang, Q. Chen, J. Ding, Verification of icephobic/anti-icing properties of a superhydrophobic surface, ACS Appl. Mater. Interfaces 5 (2013) 3370–3381, https://doi.org/10.1021/am400429q.
[45] X. Liu, H. Chen, W. Kou, D. Zhang, Robust anti-icing coatings via enhanced superhydrophobicity on fiberglass cloth, Cold Reg. Sci. Technol. 138 (2017) 18–23, https://doi.org/10.1016/j.coldregions.2017.03.004.
[46] S. Farhadi, M. Farzaneh, S.A. Kulinich, Anti-icing performance of superhydrophobic surfaces, Appl. Surf. Sci. 257 (2011) 6264–6269, https://doi.org/10.1016/j.apsusc.2011.02.057.
[47] E. Rahimi, A. Rafsanjani-Abbasi, A. Davoodi, A. Kiani-Rashid, Shape evolution of water and saline droplets during icing/melting cycles on superhydrophobic surface, Surf. Coating. Technol. 333 (2018) 201–209, https://doi.org/10.1016/j.surfcoat.2017.10.083.
[48] L. Cao, A.K. Jones, V.K. Sikka, J. Wu, D. Gao, Anti-icing superhydrophobic coatings, Langmuir 25 (2009) 12444–12448, https://doi.org/10.1021/la902882b.
[49] D. Mangini, C. Antonini, M. Marengo, A. Amirfazli, Runback ice formation mechanism on hydrophilic and superhydrophobic surfaces, Cold Reg. Sci. Technol. 109 (2015) 53–60, https://doi.org/10.1016/j.coldregions.2014.09.012.
[50] M.J. Kreder, J. Alvarenga, P. Kim, J. Aizenberg, Design of anti-icing surfaces: smooth, textured or slippery? Nat. Rev. Mater. 1 (2016) 15003, https://doi.org/10.1038/natrevmats.2015.3.
[51] C. Stamatopoulos, J. Hemrle, D. Wang, D. Poulikakos, Exceptional anti-icing performance of self-impregnating slippery surfaces, ACS Appl. Mater. Interfaces 9 (2017) 10233–10242, https://doi.org/10.1021/acsami.7b00186.
[52] Y. Liu, L. Ma, W. Wang, A.K. Kota, H. Hu, An experimental study on soft PDMS materials for aircraft icing mitigation, Appl. Surf. Sci. 447 (2018) 599–609, https://doi.org/10.1016/j.apsusc.2018.04.032.
[53] R.M. Waldman, H. Li, H. Guo, L. Li, H. Hu, An experimental investigation on the effects of surface wettability on water runback and ice accretion over an airfoil surface, in: 8th AIAA Atmos. Sp. Environ. Conf., 2016, https://doi.org/10.2514/6.2016-3139.
[54] M. Pourbagian, W.G. Habashi, Surrogate-based optimization of electrothermal wing anti-icing systems, J. Aircr. 50 (2013) 1555–1563, https://doi.org/10.2514/1.C032072.
[55] L. Gao, Y. Liu, C. Kolbakir, H. Hu, An experimental investigation on an electric-thermal strategy for wind turbines icing mitigation, in: 2018 Atmos Sp Environ Conf, 2018, pp. 1–14, https://doi.org/10.2514/6.2018-3658.
[56] M. Papadakis, G.W. Zumwalt, R. Elangonan, G.A.J. Freund, M. Breer, L. Whitmer, An Experimental Method for Measuring Water Droplet Impingement Efficiency on Two- and Three-Dimensional Bodies, 1989.
[57] Y. Liu, L. Li, H. Li, H. Hu, An experimental study of surface wettability effects on dynamic ice accretion process over an UAS propeller model, Aerosp. Sci. Technol. 73 (2018) 164–172, https://doi.org/10.1016/J.AST.2017.12.003.
[58] R. Waldman, H. Hu, High-speed imaging to quantify the transient ice accretion process on a NACA 0012 airfoil, in: 53rd AIAA Aerosp. Sci. Meet., 2015. AIAA 2015-0033.
[59] R.M. Waldman, H. Li, H. Hu, An experimental investigation on the effects of surface wettability on water runback and ice accretion over an airfoil surface, in: 8th AIAA Atmos. Sp. Environ. Conf, American Institute of Aeronautics and Astronautics, Virginia, 2016, https://doi.org/10.2514/6.2016-3139.
[60] L. Gao, Y. Liu, H. Hu, An Experimental Study on Icing Physics for Wind Turbine Icing Mitigation, 2017, pp. 1–16, https://doi.org/10.2514/6.2017-0918.
[61] Y. Liu, H. Hu, An experimental investigation on the unsteady heat transfer process over an ice accreting airfoil surface, Int. J. Heat Mass Transf. 122 (2018) 707–718, https://doi.org/10.1016/J.IJHEATMASSTRANSFER.2018.02.023.
[62] W.A. Timmer, R.P.J.O.M. van Rooij, Summary of the delft university wind turbine dedicated airfoils, J. Sol. Energy Eng. 125 (2003) 488, https://doi.org/10.1115/1.1626129.
[63] R.P.J.O.M. van Rooij, W.A. Timmer, Roughness sensitivity considerations for thick rotor blade airfoils, J. Sol. Energy Eng. 125 (2003) 468, https://doi.org/10.1115/1.1624614.
[64] L. Gao, Y. Liu, W. Zhou, H. Hu, An Experimental Study on the Aerodynamic Performance Degradation of a Wind Turbine Blade Model Induced by Ice Accretion Process, 2019, https://doi.org/10.1016/j.renene.2018.10.032.
[65] Mikron Instrument Company, Table of Emissivity of Various Surfaces, 2014, pp. 1–13. http://www-eng.lbl.gov/~dw/projects/DW4229_LHC_detector_analysis/calculations/emissivity2.pdf.
[66] A.J. Meuler, J.D. Smith, K.K. Varanasi, J.M. Mabry, G.H. McKinley, R.E. Cohen, Relationships between water wettability and ice adhesion, ACS Appl. Mater. Interfaces 2 (2010) 3100–3110, https://doi.org/10.1021/am1006035.
[67] M. Edalatpour, L. Liu, A.M. Jacobi, K.F. Eid, A.D. Sommers, Managing water on heat transfer surfaces: a critical review of techniques to modify surface wettability for applications with condensation or evaporation, Appl. Energy 222 (2018) 967–992, https://doi.org/10.1016/j.apenergy.2018.03.178.
[68] J.T. Korhonen, T. Huhtamäki, O. Ikkala, R.H.A. Ras, Reliable measurement of the receding contact angle, Langmuir 29 (2013) 3858–3863, https://doi.org/10.1021/la400009m.
[69] S. Liu, H. Li, M. Song, B. Dai, Z. Sun, Impacts on the solidification of water on plate surface for cold energy storage using ice slurry, Appl. Energy (2017), https://doi.org/10.1016/j.apenergy.2017.08.012.